IEEE Access
Multidisciplinary ⋮ Rapid Review ⋮ Open Access Journal

Received 13 September 2023, accepted 29 October 2023, date of publication 6 November 2023,
date of current version 9 November 2023.

*Digital Object Identifier 10.1109/ACCESS.2023.3330431*

RESEARCH ARTICLE

# Fast Planning and Tracking of Complex Autonomous Parking Maneuvers With Optimal Control and Pseudo-Neural Networks

**EDOARDO PAGOT, MATTIA PICCININI, (Member, IEEE), ENRICO BERTOLAZZI, AND FRANCESCO BIRAL**
Department of Industrial Engineering, University of Trento, 38123 Trento, Italy
Corresponding author: Mattia Piccinini (mattia.piccinini@unitn.it)

**ABSTRACT** This paper presents a framework to plan and execute autonomous parking maneuvers in complex parking scenarios. We formulate a minimum-time optimal control problem for trajectory planning, using an indirect optimal control approach. A novel smooth penalty function is devised for collision avoidance with optimal control, and an effective technique is adopted to compute an initial solution guess. The trajectory planning tasks are solved with low computational times, and a dense mesh is used to discretize the domain of the optimal control problems, resulting in accurate collision-free solutions. The planned parking maneuvers are tracked with an original pseudo-neural feedforward-feedback steering controller, which outperforms other techniques from the literature, and a feedback longitudinal controller, to drive a realistic 14-degree-of-freedom vehicle simulator. We validate the planning and tracking algorithms in challenging narrow parking scenarios, including reverse, parallel and angle parking, and unstructured environments. The framework robustness is assessed by changing the vehicle mass, the road adherence conditions, and by introducing measurement noise with realistic sensor models. A video of the trajectory planning and tracking results is available as supplementary material.

**INDEX TERMS** Autonomous parking, optimal control, trajectory optimization, trajectory tracking.

## I. INTRODUCTION

Current developments in intelligent vehicle technology focus on several aspects of autonomous driving, including autonomous parking and valet parking. Valet parking is the ability to autonomously cruise for a free parking spot, while autonomous parking refers more specifically to the execution of a parking maneuver. This paper focuses on planning and executing autonomous parking maneuvers.

The expected benefits of autonomous parking and valet parking are several. There are technical advantages, such as the ability to move and park in narrower spaces, compared to human-driven parking. Moreover, an autonomous system can find the fastest and shortest parking path, and it can minimize the time to search for a parking spot—which is anything but a minor matter. In the New York City region alone, vehicles cruising for a free parking space travel more than 70,000 miles every day. This equals to a daily emission of 29 metric tons of $CO_2$ [1]. Hence, autonomous parking systems can considerably impact greenhouse emissions. There are also advantages related to passenger comfort: for example, a passenger can exit the vehicle and let it look for a parking spot by itself. The vehicle could be parked in narrow spots where the driver is precluded from opening the doors, or where drivers with reduced mobility would not be able to dismount from the vehicle.

An autonomous parking framework usually consists of three main functional parts: (a) environment mapping and on-line vehicle state estimation; (b) trajectory planning, to compute a feasible path and velocity profile; (c) motion tracking, to execute the planned trajectory. In this work, we focus on trajectory planning and tracking (points (b)

The associate editor coordinating the review of this manuscript and approving it for publication was Wonhee Kim.

and (c)), but we finally analyze the robustness of our framework to measurement noise, in a realistic mapping and state estimation simulation scenario.

The following subsection critically analyses the strengths and limitations of related literature papers, after which the main paper contributions are outlined.

### A. RELATED WORK

In the field of path and trajectory planning for automated parking, the main techniques that emerge in the literature [2] are search-based, sampling-based, and optimal control-based. The search methods, like the many variants of A* and Hybrid A* [3], [4], and the sampling RRT*-like techniques [5], [6] tend to suffer from curse of dimensionality issues, when the parking spaces are narrow and a fine map resolution is required [2], [7]. Moreover, the search A*-like methods are generally used for *path planning*, and the computed path may be far from the global optimum. Conversely, optimal control-based methods can be used for *trajectory planning*, i.e., to compute both a path and a velocity profile. The computed trajectory is at least locally optimal, according to the chosen objective function, constraints, and vehicle dynamics model.

In recent years, several authors used optimal control (OC) to solve trajectory planning problems for autonomous parking. The authors of [8] used optimal control and direct collocation to compute minimum-time parking maneuvers in generic scenarios with multiple obstacles; however, their computational times were far from real-time. The previous work was then extended in [9], in which a look-up table of pre-computed OC solutions was created and provided as guess for the minimum-time optimal control problem. The framework was successfully tested on narrow parking spots; however, only the parallel parking scenario was studied, and the computational times were in the order of 40-180 seconds, thus far-fetched for a real-time application. In [10], the authors obtained the parking maneuvers from the solution of a combined minimum-time and minimum-space optimal control problem (OCP). The OCP was initialized by means of standard maneuvers from a look-up table. They tuned and tested their framework on reverse parking only, and the computational times were in the order of 100 seconds. In [11], a multi-stage Hybrid A* was developed to compute a coarse path in unstructured parking scenarios, and the solution was refined by solving an optimal control problem in an obstacle-free corridor. Similarly, [12] used an enhanced Hybrid A* method to compute an obstacle-free corridor, in which an OCP was solved for valet parking navigation problems. The authors of [13] presented an iterative framework for autonomous parking, based on the direct optimal control method. They reported promising computational times lower than 1 second; however, the framework was validated on quite trivial scenarios, that were closer to a navigation problem than to a parking one. The authors of [14] developed a machine learning (ML) framework based on a Monte Carlo tree search, able to learn optimal parking maneuvers. The ML algorithm was trained with the solutions of minimum-time optimal control problems solved with direct collocation, which were computed offline; the computational time for the offline solution of the OCPs is not provided by the authors, and the framework was tested only on parallel parking scenarios.

Recently, some papers used reinforcement learning [15], [16] for trajectory planning in autonomous parking. However, they showed only examples of parallel parking scenarios.

Finally, a remarkable application of optimal control for autonomous parking is [17], where the authors solved a minimum-time OCP with a convexification technique, in order to obtain an exact and smooth formulation of the original, non-convex OCP. They employed the Hybrid $A^*$ algorithm [3] to compute solution guesses for the optimal control problem, obtaining average computational times lower than 2-3 seconds, and testing their framework on both reverse and parallel parking scenarios. However, the parking spots were relatively large, and the resulting parking maneuvers were quite simple, being always composed of only two driving segments, the first in the forward direction, and the second in the rearward direction. Moreover, to reduce the computational time, the discretization grid of the OCP was quite coarse: as pointed out by the authors, some collisions with the obstacles are visible in the plotted OCP solutions, in the time frame between two consecutive discretization grid points.

To summarize, the main difficulties that hinder accurate and computationally fast OC trajectory planning for autonomous parking are typically related to: (1) the need to use a dense discretization planning grid; (2) the need to plan complex maneuvers, with many segments in the forward and rearward direction; (3) the non-convexity of the planning domain; (4) the presence of many local minima, and hence the need for a good solution guess.

Regarding the closed-loop motion tracking and execution of parking or low-speed maneuvers, various low-level controllers can be found in the literature [18], [19], [20], [21]. For example, in [6] a pure-pursuit steering controller [22] was used for path tracking, and a PI longitudinal controller for speed tracking. The authors in [23] used a short-horizon MPC to track a given parking trajectory. They linearized a kinematic vehicle model around the reference trajectory, obtaining a quadratic problem to be solved online. A sliding mode path tracking controller was used in [24], in combination with a PI speed tracking regulator. Other authors used prescribed performance function-based controllers for trajectory tracking with collision avoidance [25], [26]. A Lyapunov-based feedback controller was presented [27], for both speed and path tracking. In [28], an integrated longitudinal-lateral neural network controller for autonomous parking was developed. However, their approach requires a very large training dataset, since the neural network structure is generic, and they show only parallel parking examples.

### B. RESEARCH QUESTION

The research question of our paper is the following: *Given a high-fidelity vehicle simulator, develop a framework for online fast trajectory planning with optimal control and low-level tracking of complex automated parking maneuvers. The framework must operate in a variety of real-life parking scenarios, including narrow parallel, reverse and angle parking spots, and unstructured environments. The trajectory tracking algorithms must be sufficiently robust to unknown variations in the vehicle's parameters and road adherence, and to measurement noise.*

To the best of our knowledge, no existing literature paper answers the previous research question in its entirety. More precisely, the works mentioned in Section I-A are limited by at least one of the following factors:

1) Real-time optimal control planning and tracking of accurate parking maneuvers was not performed in both narrow parallel/reverse/angle parking spots and unstructured environments. Specifically, the authors of [17] solved their OCPs with acceptable computational times, but they used a quite coarse discretization mesh, which yielded local obstacle collisions in narrow parking spots. The authors of [11] dealt with generic parking scenarios, but they solved the OCP in an obstacle-free corridor, and without very narrow parking spots.
2) Many authors, like [9], [10], [11], and [17], focused mainly on trajectory planning, but they did not properly analyze the maneuver execution phase, with high-fidelity multibody vehicle simulators. Moreover, they did not consider model mismatches and sensor noise.
3) Most of the optimal control-based papers used direct collocation approaches, while indirect optimal control methods —based on the Pontryagin's Maximum Principle (PMP)— are still unexplored in the field of autonomous parking.
4) Some papers, like [28], used neural network controllers for motion tracking, but they required very large training datasets, and they focused on a limited set of parking scenarios.

### C. PAPER CONTRIBUTION AND STRUCTURE

Our paper aims to answer the research question of Section I-B, through the following contributions:

1) We present a novel autonomous parking framework that solves minimum-time optimal control problems (OCPs) by means of an indirect method. Our framework is able to deal with narrow parking spots and generic unstructured parking scenarios, computing complex maneuvers with many forward/reverse driving segments, in a single optimization. In comparison with the direct collocation literature methods, we employ an indirect optimal control method, implemented by our software tool PINS. Using PINS and an effective OCP formulation, low computational times are obtained even with a dense discretization time grid, that yields accurate solutions near the obstacles.
2) We devise a novel method to deal with collision avoidance in the optimal control problems, using penalty functions described as smooth three-dimensional functions. Our formulation allows the creation of arbitrary scenarios, by approximating obstacle shapes using multiple rectangles of different sizes.
3) A novel scheme is adopted to generate the solution guess for the OCP, combining a Hybrid A* algorithm and an optimal control tracking problem.
4) An original pseudo-neural physics-driven steering controller is devised, which enables an accurate closed-loop tracking of the optimal control trajectories on a complex 14-degree-of-freedom vehicle simulator.
5) The parking framework (planning and tracking) is validated on a wide range of complex and non-conventional maneuvers, compared to what is available in the literature. Moreover, we analyze the framework's robustness to changes in vehicle parameters and road adherence, and to localization noise due to sensors.

This paper is organized as follows. Section II presents an overview of the trajectory planning and control framework, and of the vehicle simulator to be controlled. Section III outlines the optimal control problem formulation for trajectory planning, and the warm-start strategy to generate a good guess for the problem. Section IV deals with the trajectory tracking controllers, with a special focus on the pseudo-neural feedforward-feedback steering controller. The main results are described in Section V: we first analyze the planned and executed maneuvers in a wide range of challenging parking scenarios. Then, we evaluate the framework's robustness to variations in the vehicle parameters and road adherence, and to vehicle's localization errors due to measurement noise. Finally, in Section VI we outline our conclusions and the future work.

## II. FRAMEWORK OVERVIEW

In this section, we give an overview of the presented autonomous parking framework. The trajectory planning and tracking scheme is provided in Fig. 2. The framework plans and executes parking maneuvers with a custom-designed vehicle simulator (VS), which accurately reproduces the dynamics of a sedan car.

### A. VEHICLE SIMULATOR

With the target to reproduce the dynamical behavior of a real sedan car, the VS is implemented as a high-fidelity 14-degree-of-freedom multibody model. The Pacejka MF-6.2 formulation [29] is adopted for the tire forces and moments, and the VS can be used on three-dimensional roads [30]. The vehicle suspensions are modeled with kinematic and compliance maps. An efficient formulation is obtained for the VS multibody model through symbolic manipulation,

**FIGURE 1.** Vehicle driving simulator in the Autonomous Driving Laboratory of the University of Trento (Italy). The simulator uses real-time hardware to implement the presented VS model.

**TABLE 1.** Main parameters of the vehicle simulator.

| Parameter | Symbol | Value |
|---|---|---|
| Vehicle mass | $m$ | 1300 kg |
| Center of mass (CoM) height | $h_G$ | 0.285 m |
| Front axle distance from the CoM | $L_1$ | 1.225 m |
| Rear axle distance from the CoM | $L_2$ | 1.375 m |
| Wheelbase | $L$ | 2.60 m |
| Yaw inertia | $I_z$ | 1400 kg m$^2$ |
| Track width (front) | $W_1$ | 1.80 m |
| Track width (rear) | $W_2$ | 1.80 m |
| Steering ratio | $\tau_d$ | 20 |

so that the VS supports real-time hardware-in-the-loop (HIL) simulations.

The VS is integrated into the driving simulator of Fig. 1, in the Autonomous Driving Laboratory at the University of Trento (Italy). The VS employed in this paper was also used in [31], to validate an artificial race driver, with minimum-time maneuvers. The reader is referred to [32, Sections V-VI] for further implementation details about the VS. The VS simulates a front-wheel-drive (FWD) sedan car, with an electric motor and an open mechanical differential. The main parameters of the VS are reported in Table 1.

In this work, the internal structure and the parameters of the VS are assumed to be unknown, so that the VS is used as a black-box model. Moreover, we will test the robustness of our autonomous parking framework by varying some parameters of the VS (vehicle mass and road adherence), without changing/re-training the models for trajectory planning and control.

We stress that the use of a high-fidelity VS is pivotal in the development of autonomous parking systems, as it effectively reduces testing costs and accelerates the design iterative process.

### B. TRAJECTORY PLANNING AND CONTROL OVERVIEW

Given the desired initial and final vehicle pose, and the positions of the obstacles, an optimal control problem (OCP) plans the parking trajectory (path and speed profile). A feedforward steering controller is implemented with a novel pseudo-neural physics-driven structure. Such a pseudo-neural controller computes the steering angle $\delta_{\mathrm{ff}_k}$ for the current time step $k$, using a window of present and future optimal trajectory curvature values $[\rho_k, \ldots, \rho_{k+q}]$. A feedback steering proportional controller computes a steering angle $\delta_{\mathrm{fb}_k}$, to compensate the path $(x, y)$ and yaw angle $(\theta)$ tracking errors. The total steering wheel angle is computed as $\delta_{D_k} = \delta_{\mathrm{ff}_k} + \delta_{\mathrm{fb}_k}$, and it is an input for the VS. Finally, a feedback longitudinal PI controller is used to track the optimal forward speed $v_x$ profile, computing the requested pedal $p$, with $-1 \leq p \leq 1$ ($p < 0$ for braking, $p > 0$ for throttle).

The optimal control problem is solved only once, before the maneuver is executed, but we will show that the computational times are low enough for a real-world application. During the maneuver execution, the optimal control solution is extracted and fed to the feedforward and feedback tracking controllers, which operate in real-time at 1 kHz. The vehicle simulator is also executed at 1 kHz.

In Section V-D, we will test the planning and control scheme of Fig. 2 in a realistic localization and state estimation simulation framework, to evaluate the scheme's robustness to measurement errors.

## III. TRAJECTORY PLANNING

This section describes the OCP employed for trajectory planning, the novel penalty function for collision avoidance, and the original method to generate a guess solution for the OCP.

### A. VEHICLE MODEL FOR OPTIMAL CONTROL

In the optimal control problem formulation, we adopt a kinematic model of the vehicle motion:

$$\begin{cases} \dot{x}(t) = v_x(t)\cos(\theta(t)) & \text{(1a)} \\ \dot{y}(t) = v_x(t)\sin(\theta(t)) & \text{(1b)} \\ \dot{\theta}(t) = v_x(t)\tan(\delta(t))/L & \text{(1c)} \\ \dot{v}_x(t) = a_x(t) & \text{(1d)} \\ \tau_\delta \dot{\delta}(t) = \delta_{\mathrm{dot}}(t) & \text{(1e)} \end{cases}$$

where the notation $\dot{\mathrm{x}}$ indicates the derivative of the quantity x with respect to time $t$. Referring to Fig. 3, $x$ and $y$ are the coordinates of the origin of the vehicle's moving frame —centered on the vehicle's rear axle—, with respect to the ground frame X-Y. The angle $\theta$ is the orientation of the vehicle's moving frame, with respect to the ground frame. $v_x$ is the vehicle forward velocity, while $\delta$ is the Ackermann steering angle (at the center of the front axle). The model states are $\boldsymbol{x} = [x, y, \theta, v_x, \delta]$, while the controls are $\boldsymbol{u} = [a_x, \delta_{\mathrm{dot}}]$, where $a_x$ is the vehicle forward acceleration and $\delta_{\mathrm{dot}}$ is the angular velocity of the steering wheel. The parameter $\tau_\delta$ in (1e) is the transmission ratio of the steering mechanism. A reasonable limit on $\delta_{\mathrm{dot}}$ is imposed in order to consider the maximum angular speed reachable by real-world electric steering wheel actuators. Finally, $L$ is the vehicle wheelbase.

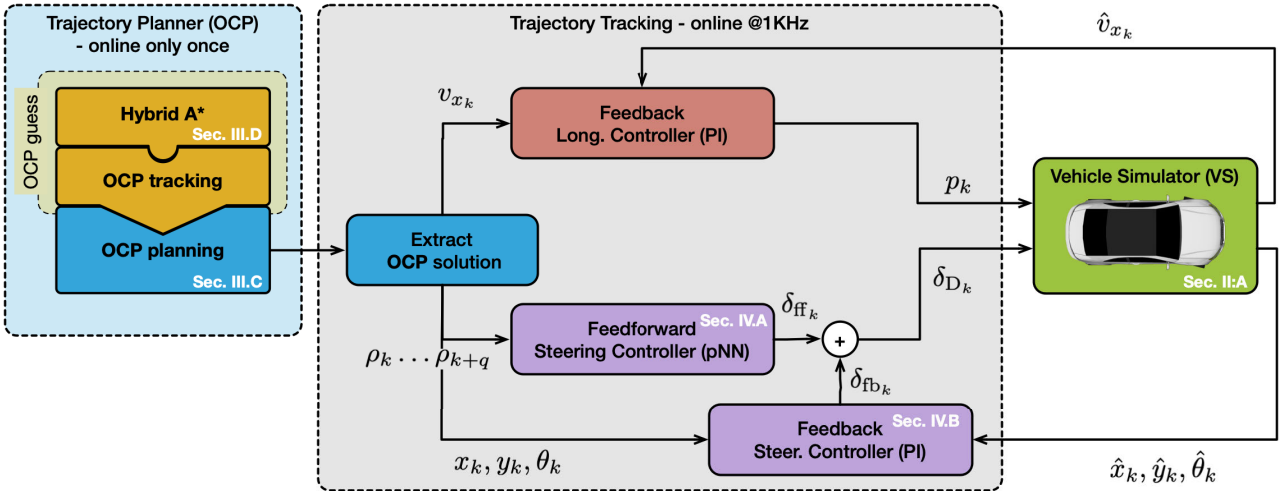


**FIGURE 2.** Overview of the trajectory planning and tracking framework. The OCP plans the parking trajectory only once, with low computational times, and the maneuver is then tracked by the feedforward and feedback controllers at a 1 kHz rate. In each control block, we write the paper section that describes it.

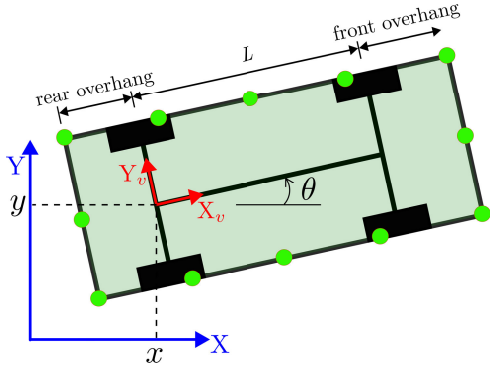


**FIGURE 3.** Schematic of the ego vehicle: the quantities $\{x, y\}$ and $\theta$ represent the position and orientation of the vehicle's moving frame $X_v$-$Y_v$ (in red), with respect to the ground frame X-Y (in blue). The green dots are the collision checking points used to evaluate the obstacle penalties. The vehicle wheelbase is $L$. Notice that the front and rear overhangs of the vehicle are considered in the model.

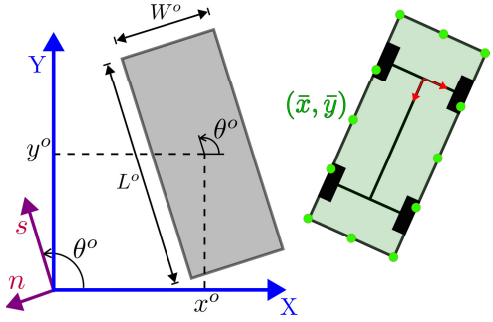


**FIGURE 4.** In the optimal control problem, an obstacle (depicted in grey) is modeled using its absolute position $[x^o, y^o]$ and orientation $\theta^o$, with respect to the X-Y ground frame, and its width $W^o$ and length $L^o$. The penalty function $P(\cdot)$ in (2) takes as input the obstacle geometry and one of the collision checking points $[\bar{x}, \bar{y}]$ (green dots), belonging to the ego vehicle and expressed in the X-Y ground frame. The reference frame $s$-$n$ is rotated by the obstacle orientation angle $\theta^o$, and is used to ease collision checking with generically oriented obstacles.

We underline that the steering angle $\delta$ computed by the OCP with the kinematic model (1c,1e) is *not* directly used to control the vehicle simulator, whose steering dynamics is more complex and nonlinear. Section IV-A will present a feedforward steering controller, which is designed and trained to learn a more accurate model of the steering dynamics, to track the trajectory curvature profile returned by the OCP.

### B. OBSTACLE FORMULATION FOR OPTIMAL CONTROL

We introduce a novel penalty function to deal with collision avoidance in the optimal control problem. The penalty function enforces the geometry of a given obstacle: referring to Fig. 4, an obstacle (shown in grey) is defined in terms of its absolute position $[x^o, y^o]$, orientation $\theta^o$, width $W^o$ and length $L^o$. The arguments of the penalty function are the obstacle geometry parameters and the coordinates $[\bar{x}, \bar{y}]$ of an arbitrary point. As will be explained next, the points $[\bar{x}, \bar{y}]$ passed as arguments of the penalty function belongs to a set of several collision checking points defined along the ego vehicle's perimeter (green dots in Fig. 4). The penalty function is named $P(\cdot)$, and is expressed as:

$$P(\bar{x}, \bar{y}, x^o, y^o, \theta^o, W^o, L^o) = Q(\bar{s}, L^o, s^o) \cdot Q(\bar{n}, W^o, n^o) \tag{2}$$

$$\text{with} \begin{cases} [\bar{s}, \bar{n}]^T = \mathbf{R}(\theta^o) \cdot [\bar{x}, \bar{y}]^T & \text{(3a)} \\ [s^o, n^o]^T = \mathbf{R}(\theta^o) \cdot [x^o, y^o]^T & \text{(3b)} \end{cases}$$

To consider the obstacle orientation angle $\theta^o$, equations (3a,3b) are used to perform a change of reference frame: the collision checking point $[\bar{x}, \bar{y}]$ and the obstacle center $[x^o, y^o]$, defined in the ground frame X-Y, are now expressed in the rotated $s$-$n$ frame (Fig. 4). In (3a,3b), the notation $[\cdot]^T$

indicates the transpose of a vector, while the rotation matrix $\mathbf{R}(\theta^{\mathbf{o}})$ is given by:

$$\mathbf{R}(\theta^{\mathbf{o}}) = \begin{bmatrix} \cos(\theta^o) & \sin(\theta^o) \\ -\sin(\theta^o) & \cos(\theta^o) \end{bmatrix} \tag{4}$$

The penalty $P(\cdot)$ in (2) is built by multiplying two smooth functions, named $Q(\cdot)$ and plotted in Fig. 5a. The $Q(\cdot)$ functions use as arguments the transformed coordinates of the collision checking point $[\bar{s}, \bar{n}]$ and of the obstacle center $[s^o, n^o]$, computed with (3a,3b). As shown in Fig. 5a, the value of the function $Q(\bar{s}, L^o, s^o)$ increases if $s^o - \frac{L^o}{2} \leq \bar{s} \leq s^o + \frac{L^o}{2}$, i.e., if the collision checking point is inside the obstacle shape, along the $s$ direction.

The function $Q(\cdot)$ is computed as the first-order derivative of a smooth *Clip* function, and is written as[1]:

$$\begin{aligned} &Q(\bar{s},\ L^o,\ s^o) \\ &= \frac{1}{2\,h_t}\left(\bar{s} - s_0 + \frac{L^o}{2}\right)\frac{1}{\sqrt{1 + \frac{1}{h_t{}^2}\left(\bar{s} - s_0 + \frac{L^o}{2}\right)^2}} + \\ &\quad - \frac{1}{2\,h_t}\left(\bar{s} - s_0 - \frac{L^o}{2}\right)\frac{1}{\sqrt{1 + \frac{1}{h_t{}^2}\left(\bar{s} - s_0 - \frac{L^o}{2}\right)^2}} \end{aligned} \tag{5}$$

where $h_t$ is a tunable smoothing parameter, whose effect is shown in Fig. 5a. The function $Q(\cdot)$ in (5) is computed along the $s$ direction: by changing its arguments, the function is also evaluated along the $n$ direction, and used in (2). Fig. 5b shows an example of the obstacle penalty function $P(\cdot)$, obtained with (2) and $[x^o, y^o] = [0, 0]$ m, $\theta^o = 0$ deg, $W^o = 2$ m, $L^o = 3$ m. Note that, when $\theta^o = 0$ deg, the obstacle $s$-$n$ directions are aligned with the ground reference frame X-Y (Fig. 4). The penalty function in (2) models the rectangular bounding box of an obstacle. However, combining multiple penalties allows us to deal with obstacles of generic shapes, as will be shown in the angle parking example of Section V-A.

Finally, for collision checking we define 12 points on the rectangular bounding box of the ego vehicle (green dots in Fig. 3 and Fig. 4): the 4 corners of the box, 3 points equally spaced along the right and left sides of the vehicle, and the 2 middle points of the front and rear edges of the box. To consider the $i$-th obstacle, located in $[x_i^o, y_i^o]$ with orientation $\theta_i^o$ and dimensions $W_i^o$, $L_i^o$, we augment the cost function of the OCP (Section III-C) with the sum of the values of the penalty $P(\bar{x}(t), \bar{y}(t), x_i^o, y_i^o, \theta_i^o, W_i^o, L_i^o)$, evaluated in the time-varying coordinates $[\bar{x}(t), \bar{y}(t)]$ of each of the 12 points of the ego vehicle. The choice of 12 points for collision checking ensures that the bounding box of the ego car does not collide with the obstacles. The value of each penalty is zero when the corresponding collision checking point is outside the obstacle bounding box, and greater than zero if the collision checking point is inside the obstacle area. Local collisions of the ego bounding box with an obstacle could still happen in between two collision checking points; however, in our results we never encountered this event. Indeed, we started our experiments with only 4 points, and the number of 12 collision checking points represents the lower bound for which no collisions occurred, in all the test scenarios of this paper.

[1]We can tune the maximum value of the function $Q(\cdot)$ by means of an additional scaling function, here not reported for brevity.

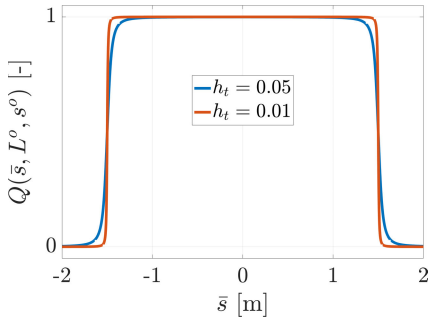


(a)

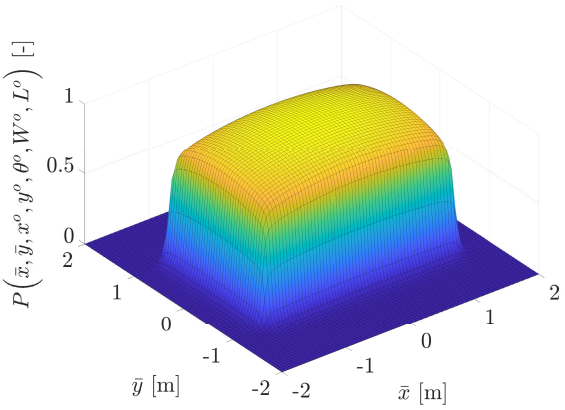


(b)

**FIGURE 5.** (a) Example of $Q(\bar{s}, L^o, s^o)$ function (5), used for collision avoidance along the obstacle longitudinal $s$ direction. The plotted example uses $s^o = 0$ m and $L^o = 3$ m: the function $Q(\cdot)$ increases if $s^o - \frac{L^o}{2} \leq \bar{s} \leq s^o + \frac{L^o}{2}$, i.e., if the collision checking point is inside the obstacle shape, along the $s$ direction. (b) Example of the three-dimensional obstacle penalty function (2), with parameters $x^o = 0$ m, $y^o = 0$ m, $\theta^o = 0$ deg, $W^o = 2$ m, $L^o = 3$ m. The value of the penalty is zero when the collision checking point coordinates $[\bar{x}, \bar{y}]$ are outside the obstacle bounding box, and greater than zero when the coordinates $[\bar{x}, \bar{y}]$ are inside the obstacle area.

### C. OPTIMAL CONTROL PROBLEM FORMULATION

Exploiting the devised collision avoidance penalty function, we solve the following optimal control problem for trajectory planning of parking maneuvers:

$$\min_{\boldsymbol{u} \in \mathcal{U}} w_T t_f + \int_0^{t_f} \ell_{\text{obst}}(t)\,\mathrm{d}t \tag{6a}$$

$$\text{s.t. } \dot{\boldsymbol{x}}(t) = \boldsymbol{f}(\boldsymbol{x}(t), \boldsymbol{u}(t)) \tag{6b}$$

$$|\delta(t)| \leq \delta_{\max},\ |v_x(t)| \leq v_{x_{\max}} \tag{6c}$$

$$|\delta_{\text{dot}}(t)| \leq \delta_{\text{dot}_{\max}},\ |a_x(t)| \leq a_{x_{\max}} \tag{6d}$$

$$x(0) = x_{\text{ini}},\ y(0) = y_{\text{ini}},\ \theta(0) = \theta_{\text{ini}},\ v_x(0) = 0 \tag{6e}$$

$$x(t_f) = x_f,\ y(t_f) = y_f,\ \theta(t_f) = \theta_f,\ v_x(t_f) = 0 \tag{6f}$$

We remark that the problem (6a)-(6f) is *not* formulated to track a pre-calculated path, but rather to freely plan a collision avoidance trajectory. The cost function (6a) has two main purposes: minimize the maneuver time $t_f$, and avoid collisions. The former goal is weighted by the tunable parameter $w_T$. Collision avoidance is performed with the integral term in (6a), where $\ell_{\text{obst}}(t)$ has the following expression:

$$\ell_{\text{obst}}(t) = \sum_{i=1}^{n_{\text{obs}}} \sum_{j=1}^{n_{\text{pts}}} P\big(x_j(t), y_j(t), x_i^o, y_i^o, \theta_i^o, W_i^o, L_i^o\big) \tag{7}$$

$\ell_{\text{obst}}(t)$ in (7) is the sum of the values of the novel penalty function $P(\cdot)$, computed for all the $n_{\text{pts}} = 12$ collision checking points of the ego vehicle (Fig. 3), and for all the $n_{\text{obs}}$ obstacles. In (7), $[x_j(t), y_j(t)]$ are the coordinates of the $j$-th collision checking point of the ego vehicle; $[x_i^o, y_i^o, \theta_i^o]$ are the coordinates and orientation of the $i$-th obstacle, whose width and length are $W_i^o$ and $L_i^o$. The expression of the penalty function $P(\cdot)$ is given by (2). The relative weight between the two objectives in the cost function (6a) is tuned so that no collisions occur, in all the 75 maneuvers on which the framework is tested. Also, the absolute weight on the final-time objective $w_T$ is large enough to enforce parking maneuver times that are well inside the range of human drivers' parking times.

The dynamical system (6b) is the kinematic vehicle model (1a). Box constraints (6c,6d) are imposed for the states $\{\delta, v_x\}$ and the controls $\{\delta_{\text{dot}}, a_x\}$. Initial and final conditions are set for the vehicle pose and velocity with the constraints (6e,6f). Since we employ an indirect optimal control method, such initial and final conditions are strictly enforced.

Notice that, in the optimal control formulation (6a)-(6f), the final maneuver time $t_f$ is not known a priori, while being one of the quantities we want to minimize. In order to solve the OCP, we rewrite it in its *free-time* formulation, by substituting the time $t$ with a new independent variable, named $\zeta$:

$$t = \zeta\, t_f, \qquad \zeta \in [0, 1], \tag{8}$$

The new independent variable $\zeta$ ranges in the fixed interval $[0, 1]$. The final maneuver time $t_f$ is now treated as a new state variable, which is constant in time, i.e. $\frac{\mathrm{d}t_f}{\mathrm{d}t} = 0$. The extended state of the dynamical system is redefined as $\boldsymbol{x} = [x, y, \theta, v_x, \delta, t_f]$. Let us indicate with $h'$ the derivative of the generic quantity $h$ with respect to the new independent variable $\zeta$. Using the chain rule of differentiation, we can write:

$$\boldsymbol{x}' = \frac{\mathrm{d}\boldsymbol{x}}{\mathrm{d}\zeta} = \frac{\mathrm{d}\boldsymbol{x}}{\mathrm{d}t}\frac{\mathrm{d}t}{\mathrm{d}\zeta} = \frac{\mathrm{d}\boldsymbol{x}}{\mathrm{d}t} t_f \tag{9}$$

Exploiting the relation (9) and adding the new state variable $t_f(\zeta)$, whose derivative with respect to $\zeta$ is zero, the system (1a) is rewritten as:

$$\begin{cases} x'(\zeta) = t_f(\zeta)\, v_x(\zeta) \cos\left(\theta(\zeta)\right) \\ y'(\zeta) = t_f(\zeta)\, v_x(\zeta) \sin\left(\theta(\zeta)\right) \\ \theta'(\zeta) = t_f(\zeta)\, v_x(\zeta) \tan(\delta(\zeta))/L \\ v_x'(\zeta) = t_f(\zeta)\, a_x(\zeta) \\ \tau_\delta \delta'(\zeta) = t_f(\zeta)\, \delta_{\text{dot}}(\zeta) \\ t_f'(\zeta) = 0 \end{cases} \tag{10}$$

and the original OCP (6a)-(6f) is reformulated as:

$$\min_{\boldsymbol{u}\in\mathcal{U}} w_T t_f + \int_0^1 \ell_{\text{obst}}(\zeta)\, t_f \,\mathrm{d}\zeta \tag{11a}$$

s.t.(10)

$$|\delta(\zeta)| \le \delta_{\max}, \;\; |v_x(\zeta)| \le v_{x_{\max}} \tag{11b}$$

$$|\delta_{\text{dot}}(\zeta)| \le \delta_{\text{dot}_{\max}}, \;\; |a_x(\zeta)| \le a_{x_{\max}} \tag{11c}$$

$$x(0) = x_{\text{ini}}, \;\; y(0) = y_{\text{ini}}, \;\; \theta(0) = \theta_{\text{ini}}, \;\; v_x(0) = 0 \tag{11d}$$

$$x(1) = x_f, \;\; y(1) = y_f, \;\; \theta(1) = \theta_f, \;\; v_x(1) = 0 \tag{11e}$$

Note that the final time $t_f$ is now a state variable, thus it can be explicitly minimized in the target function (11a).

The OCP is formulated and solved using the software suite PINS [33], [34], [35], [36], [37], which is based on the indirect method for optimal control. A comprehensive comparison of direct and indirect methods for the solution of optimal control problems can be found in [37]. The comparison showed that PINS has comparable performances to a state-of-the-art direct method implementation. Starting from the continuous-time OCP (11a)-(11e), PINS builds a two-point boundary value problem, which is then discretized. We use a dense time grid with 500 points for the discretization. The choice of PINS is justified because the indirect optimal control method implemented by the proprietary software and solver, developed by our research group, allow us to solve the OCPs with low computational times on the dense mesh grid. The reader can refer to [31], [38], [39], [40], and [41] for other recent examples of minimum-time nonlinear OCPs solved in real-time and offline using PINS.

### D. TRAJECTORY GUESS GENERATION

We adopt an effective *Hybrid A* + OCP tracking* strategy to compute a solution guess for the optimal control problem. The proposed guess method combines the Hybrid A* algorithm [3] and an optimal control tracking problem. First, a kinematically feasible parking path is generated through the Hybrid A* algorithm. Second, the path provided by the Hybrid A* is tracked by solving the following optimal control problem:

$$\begin{aligned} \min_{\boldsymbol{u}\in\mathcal{U}} \; & w_T t_f + \int_0^1 \Big[ w_P \Big( \big(x(\zeta) - x_A(\zeta)\big)^2 \\ & + \big(y(\zeta) - y_A(\zeta)\big)^2 \Big) + w_\theta \big(\theta(\zeta) - \theta_A(\zeta)\big)^2 \Big] t_f \,\mathrm{d}\zeta \\ \text{s.t.} \;\; & (10),\ (11b),\ (11c),\ (11d),\ (11e) \end{aligned} \tag{12}$$

where $\{x_A, y_A, \theta_A\}$ are the coordinates and yaw angle of the Hybrid A* path, and $\{w_T, w_P, w_\theta\}$ are tunable weights. Note that the tracking OCP (12) uses the same vehicle model (10) and constraints (11b)-(11e) as the main OCP (11a)-(11e). The solution of the tracking OCP (12) is then used as a guess for the free-trajectory main optimal control problem (11a)-(11e).

As will be shown in Section V-B, our solution guess method (Hybrid A* + OCP tracking) outperforms the Hybrid A* alone, leading to collision-free trajectories and decreasing the overall computational times. More precisely, combining the Hybrid A* with the tracking OCP (12), we obtain a solution guess for *all* the variables of the free-trajectory OCP (11a)-(11e), while the Hybrid A* alone would provide only a sequence of positions and yaw angles.

## IV. TRAJECTORY TRACKING

In this section, we present the low-level trajectory tracking controllers. Referring to Fig. 2, we implement the following low-level controllers: a feedback longitudinal controller for speed-tracking, and a feedforward + feedback steering controller for path tracking.

The main novelty introduced in this paper for trajectory tracking is the feedforward steering controller, to which we dedicate the next section. The feedback steering controller consists of two proportional regulators, which will be described in Section IV-B. Finally, the feedback longitudinal controller is a simple PI regulator, and its description will be omitted since it is well established in the literature.

### A. FEEDFORWARD STEERING CONTROLLER

To track the path computed by high-level OCP, we devise a novel feedforward steering controller. The controller has a pseudo-neural physics-driven formulation (pNN), which uses few learnable parameters to accurately model the nonlinear steering dynamics.

In comparison with other papers using neural networks for motion tracking of parking maneuvers [28], the specific structure devised for pNN requires smaller training datasets to produce accurate predictions. In Section V-C, we will compare pNN with the clothoid-based [21] and pure pursuit [22] literature steering controllers. This comparison reveals that pNN significantly decreases the path and yaw angle tracking errors, and delivers smoother steering angles that improve passengers' comfort.

The design methodology of pNN is partly inspired by the neural models that we presented in [31], [42], and [43]; however, the pNN of this paper has a novel internal structure, specifically conceived to capture the nonlinear steering dynamics at low speed, for parking maneuvers.

Referring to Fig. 6, pNN computes in real-time the steering wheel angle $\delta_{\mathrm{ff}_k}$, where $k \in \mathbb{N}$ is the index of the current time step, using the following inputs:

1) a window of $q+1$ future trajectory curvature values $\boldsymbol{\rho}_k = [\rho_k, \ldots, \rho_{k+q}]$ computed by the high-level OCP;

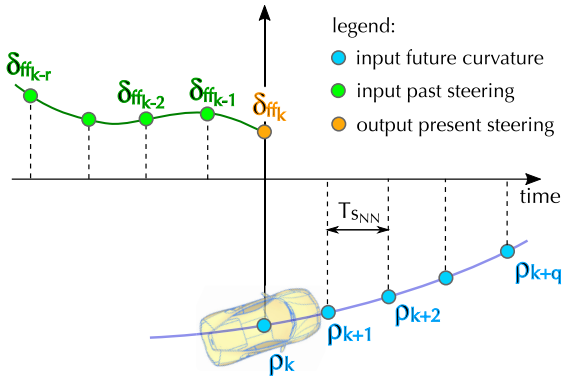


**FIGURE 6.** Inputs and output of the feedforward pseudo-neural steering controller (pNN). **Inputs:** window of future optimal curvature values $\boldsymbol{\rho_k} = [\rho_k, \ldots, \rho_{k+q}]$ computed by the OCP, and window of past steering angles $[\delta_{\mathrm{ff}_{k-r}}, \ldots, \delta_{\mathrm{ff}_{k-1}}]$ computed by pNN. **Output:** feedforward steering angle $\delta_{\mathrm{ff}_k}$ for the current time step $k$.

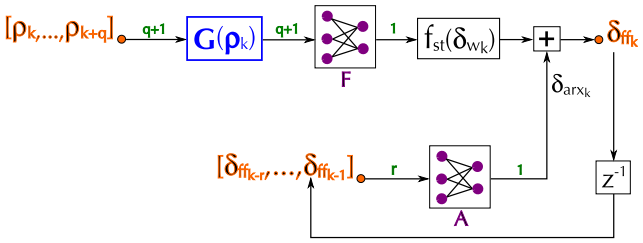


**FIGURE 7.** Structure of the feedforward pseudo-neural steering controller (pNN), aimed at modeling the nonlinear steering dynamics at low speed. The quantities colored in green are the sizes of the propagated signals.

2) a window of steering angles $[\delta_{\mathrm{ff}_{k-r}}, \ldots, \delta_{\mathrm{ff}_{k-1}}]$ computed by pNN in the past $r$ time steps.

The trajectory curvature $\rho$ used as input for pNN is given by $\Omega/v_x$, with $\Omega = \frac{\mathrm{d}\theta}{\mathrm{d}t}$ and $v_x$ being respectively the yaw rate and the forward speed computed by the high-level OCP.

pNN is a discrete-time dynamical system, with sampling time $T_{\mathrm{SNN}} = 0.05$ s, formulated as:

$$\begin{aligned}\delta_{\mathrm{ff}_k} &= f_{\mathrm{st}}\left(\boldsymbol{G}(\boldsymbol{\rho}_k)\cdot\mathbf{F}^T\right) + \left[\delta_{\mathrm{ff}_{k-r}}, \quad \ldots, \quad \delta_{\mathrm{ff}_{k-1}}\right]\mathbf{A}^T \\ &= f_{\mathrm{st}}\left(\left[g(\rho_k), \quad \ldots, \quad g(\rho_{k+q})\right]\begin{bmatrix}\mathrm{F}_1\\ \vdots \\ \mathrm{F}_{q+1}\end{bmatrix}\right) \\ &\quad + \left[\delta_{\mathrm{ff}_{k-r}}, \quad \ldots, \quad \delta_{\mathrm{ff}_{k-1}}\right]\begin{bmatrix}\mathrm{A}_1\\ \vdots \\ \mathrm{A}_r\end{bmatrix} \end{aligned} \tag{13}$$

where the notation $\mathbf{F}^T$ denotes the transpose of the vector $\mathbf{F}$. Fig. 7 graphically depicts the internal structure (13) of pNN.

Let us now analyze the role of each block in Fig. 7 and equation (13), starting from the functional layer $\boldsymbol{G}(\cdot)$.

#### 1) FUNCTIONAL LAYER $G$

The vector functional layer $\boldsymbol{G}(\boldsymbol{\rho}_k) = [g(\rho_k), \ldots, g(\rho_{k+q})]$ in (13) is designed to learn a steady-state relation between the trajectory curvature $\rho$ and the steering angle $\delta_{\mathrm{w}}$ at the

front wheels.[2] The vector $\boldsymbol{G}(\boldsymbol{\rho}_k)$ has $q+1$ entries, representing steering angle $\delta_{\mathrm{w}}$ predictions, for the present and future time steps.

The function $g(\cdot)$ is the scalar version of $\boldsymbol{G}(\cdot)$, and is designed to model a vehicle characteristic curve, which we call *curvature diagram*. Such a diagram is shown in Fig. 8b, with a solid blue line, and it can be obtained experimentally with a simple sinusoidal steering maneuver, like the one in Fig. 8a. The curvature diagram captures the deviations between $\tan(\delta_{\mathrm{w}})$ and the kinematic steering angle $\rho L$, with $L$ being the vehicle wheelbase. The shape of the diagram depends on the steering maps[3] (i.e., the nonlinear relations between the steering wheel angle $\delta_D$ and $\delta_{\mathrm{w}}$), on the characteristics of the tires and suspensions, and on other factors. The shape of the curvature diagram is nearly independent of the vehicle speed $v_x$ (in the parking range $v_x \lesssim 5$ km/h).

Let us model the curvature diagram with a polynomial, as a function of the trajectory curvature $\rho$:

$$\tan(\delta_{\mathrm{w}}) - \rho L = h(\rho) = h_1\rho + h_2\rho^3 + h_3\rho^5 \qquad (14)$$

where $h(\rho)$ is the approximating function, shown with a green line in Fig. 8b, and $\{h_1, h_2, h_3\}$ are optimization variables. Polynomials of 5$^{\text{th}}$ order (with only odd powers) were found to be accurate enough to model the curvature diagram.

The function $g(\rho)$ appearing in (13) is obtained by solving (14) for the steering angle $\delta_{\mathrm{w}}$:

$$\delta_{\mathrm{w}} = \arctan\big(h(\rho) + \rho L\big) = g(\rho) \qquad (15)$$

The function $g(\rho)$ is a static map, and relates $\rho$ with $\delta_{\mathrm{w}}$ in steady-state conditions.

### 2) FULLY-CONNECTED LAYER F

As previously described, the functional layer $\boldsymbol{G}(\boldsymbol{\rho}_k)$ returns a vector of steady-state front wheels steering angle predictions, for a given vector of present and future trajectory curvatures $\boldsymbol{\rho}_k$. The entries of $\boldsymbol{G}(\boldsymbol{\rho}_k)$ are then linearly combined by the fully-connected layer weights $\mathbf{F} = [\mathrm{F}_1, \ldots, \mathrm{F}_{q+1}]$, to model part of the transient dynamic response of the system, and improve the steady-state predictions. During training, the knowledge of the future curvature $[\rho_k, \ldots, \rho_{k+q}]$ is used to learn the dynamic behavior of the vehicle, and the possible delays between a steering input and the corresponding trajectory curvature output.

The scalar output of $\boldsymbol{G}(\boldsymbol{\rho}_k)\cdot\mathbf{F}^T$ in (13) is a first estimate of the front wheels steering angle $\delta_{\mathrm{w}_k}$, at the present time step $k$.

### 3) FUNCTIONAL LAYER $F_{\mathrm{ST}}$

The functional layer $f_{\mathrm{st}}(\cdot)$ in Fig. 7 receives as input a steering angle $\delta_{\mathrm{w}_k}$ at the front wheels —computed by the preceding layers— and maps it in the corresponding steering wheel angle $\delta_{\mathrm{ff}_k}$. More precisely, the function $f_{\mathrm{st}}(\cdot)$ is an identified static steering map,[4] i.e., a lookup table to relate $\delta_{\mathrm{w}_k}$ and $\delta_{\mathrm{ff}_k}$. Note that $f_{\mathrm{st}}(\cdot)$ is only an estimate of the real steering map, which also depends on the suspension deformations. Such minor effects are learned partly by the proposed neural model, and partly compensated by the feedback steering controller.

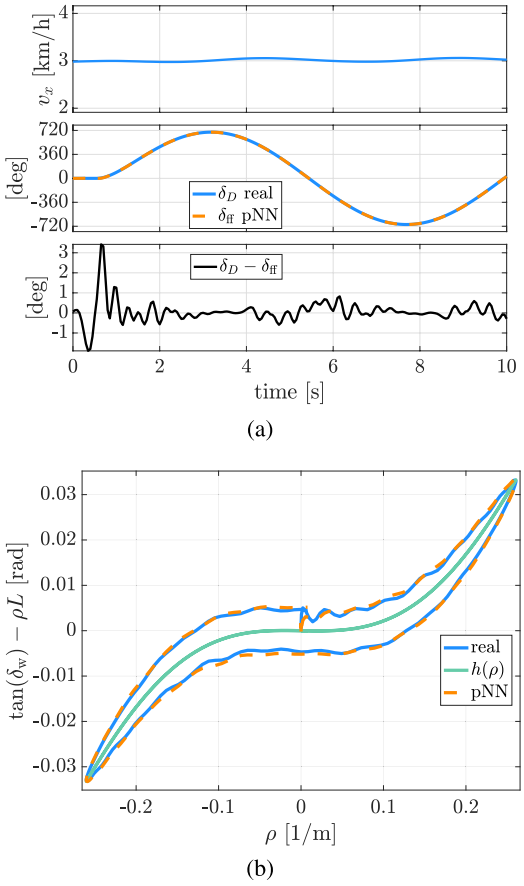


**FIGURE 8. Testing the feedforward pseudo-neural steering controller (pNN) with a sine-steer maneuver at constant speed: (a) comparison of the real steering wheel angle $\delta_D$ with the prediction $\delta_{\mathrm{ff}}$ of pNN, and (b) resulting curvature diagram.**

### 4) FULLY-CONNECTED LAYER A

Finally, in (13) we use the fully-connected layer weights $\mathbf{A} = [\mathrm{A}_1, \ldots, \mathrm{A}_r]$ to learn a linear combination of past steering angles $[\delta_{\mathrm{ff}_{k-r}}, \ldots, \delta_{\mathrm{ff}_{k-1}}]$, computed by pNN in the previous $r = 15$ time steps. The weights in $\mathbf{A}$ provide a further accuracy improvement, to model the steering dynamics. The unit delay $z^{-1}$ in Fig. 7 shows that the output of pNN is recursively fed back and re-used, in an auto-regressive way.

The output of the controller pNN is $\delta_{\mathrm{ff}_k} = f_{\mathrm{st}}(\delta_{\mathrm{w}_k}) + \delta_{\mathrm{arx}_k}$, with $\delta_{\mathrm{arx}_k} = [\delta_{\mathrm{ff}_{k-r}}, \ldots, \delta_{\mathrm{ff}_{k-1}}]\mathbf{A}^T$.

[2] $\delta_{\mathrm{w}}$ is defined as the average of the steering angles at the front wheels.

[3] The steering maps of the vehicle simulator also depend on the deformations of the suspensions.

[4] We estimate the steering map $\delta_{\mathrm{ff}} = f_{\mathrm{st}}(\delta_{\mathrm{w}})$ with offline static tests, by identifying a lookup table relating $\delta_{\mathrm{w}}$ with $\delta_{\mathrm{ff}}$. The angle $\delta_{\mathrm{w}}$ is measured as $(\delta_{11} + \delta_{12})/2$, with $\{\delta_{11}, \delta_{12}\}$ being the front right and front left wheel steering angles. Note that $\{\delta_{11}, \delta_{12}\}$ do not need to be measured online, but only one time, offline, to estimate the steering map.

#### TRAINING THE FEEDFORWARD STEERING CONTROLLER

We now provide some details about the training and parameterization of the feedforward pseudo-neural steering controller pNN.

Regarding the inputs of pNN, the lengths $q+1=15$ and $r=15$ of, respectively, the future curvature window and the past steering window are optimized with experiments, to cover a sufficient portion of the vehicle dynamic response. The pNN model has a total number of $3+(q+1)+r=3+15+15=33$ learnable parameters.

The model is trained with supervised learning. The vehicle simulator we want to control is used in an open-loop scheme to generate the training dataset: a single sinusoidal steering maneuver —like the one in Fig. 8a— is performed at a nearly constant vehicle speed (4 km/h), and the resulting vehicle telemetry is employed to train the pNN model. Similar maneuvers —with different sine steering frequency and vehicle speed— are carried out and used for the validation and test sets. The training loss function is the mean square error (MSE) between the steering wheel angles $\delta_{\text{ff}}$ computed by pNN and the recorded steering values of the training set. Tensorflow is adopted to formulate and train pNN, using the Keras API and the Nadam optimization method [44].

We underline that, given the specific structure designed for pNN and its low number of learnable parameters, the training dataset required to produce accurate predictions is smaller than in other more traditional neural network approaches [28].

Fig. 8a shows the results obtained with pNN on a test set, not used during training. The steering angle $\delta_{\text{ff}}$ computed by pNN is very close to the recorded angle $\delta_D$, and the predicted curvature diagram (Fig. 8b) is almost overlapped with the real one. The root mean squared (RMS) prediction error $\delta_{\text{ff}}-\delta_D$ on the test set is 0.487 deg.

### B. FEEDBACK STEERING CONTROLLER

The feedback steering controller consists of two proportional regulators. The first controller aims at decreasing the path tracking error,[5] namely the Euclidean distance between the (estimated) vehicle position $[\hat{x}_k, \hat{y}_k]$ at time step $k$ and the desired position $[x_k, y_k]$. The second controller reduces the difference between the (estimated) yaw angle $\hat{\theta}_k$ and the target value $\theta_k$.

The feedback controllers are tuned after training the feedforward steering controller pNN. Since the internal structure and the parameters of the vehicle to be controlled are assumed to be unknown, we tune the feedback steering controllers with a model-free approach. Similarly to what we did in [31], the M2 iterative learning tuning (ILT) method of [45] is adopted, due to its ability to deal with custom cost functions and generic plant models. Using the ILT, the proportional gain of a feedback controller is iteratively updated using an approximate gradient method, where the gradient of the cost function is estimated from the results of the previous and current iterations.

The path tracking feedback controller is tuned first, while the yaw angle tracking feedback controller is tuned in a second phase. The cost function of the ILT is a weighted sum of the mean squared values of the tracking error, the control magnitude $\delta_{\text{fb}}$, and its variations $\Delta\delta_{\text{fb}}$. In each learning iteration, the vehicle simulator is controlled in closed-loop, to track a reference parking maneuver computed with optimal control. In this way, new data are collected, the proportional controller gain is updated, and a new iteration is performed, until certain exit conditions are met.

## V. RESULTS

### A. TEST SCENARIOS

The presented autonomous parking framework is tested in four challenging scenarios. To evaluate the robustness of the trajectory planning and control algorithms, a grid of starting positions is used for each scenario:

1) *Reverse parking* scenario, Fig. 9a: the maneuvers are solved on a grid of 28 starting positions.
2) *Parallel parking* scenario, Fig. 9b: the maneuvers are solved on a grid of 21 starting positions. A nearby obstacle limits the maneuvering space on the right side of the vehicle.
3) *Generic parking* scenario, Fig. 9c: the maneuvers are solved on a grid of 14 starting positions. The vehicle must execute a reverse parking maneuver: the parking spot is quite far and an obstacle is interposed between the starting and final positions.
4) *Angle parking* scenario, Fig. 9d: the maneuvers are solved on a grid of 12 starting positions. The vehicle must reverse into an angle parking spot. The maneuvering space on the right and on the left of the vehicle is limited by a combination of obstacles. The complex obstacles in this scenario are created by rotating and superimposing several rectangular obstacles.

Overall, we use $28+21+14+12=75$ parking maneuvers to test our framework.

Considering the autonomous parking literature, our scenarios are very challenging, narrow, diverse, and representative of real-world parking situations. Moreover, our approach enables arbitrary-shaped obstacles, by overlaying multiple rectangles with different sizes and orientations. Modeling the obstacles with rectangles is therefore not a limiting choice.

Each side of the grey obstacles in Fig. 9 has a safety margin (0.10 m) with respect to the true obstacle dimensions. We underline that the safety margin is imposed only to consider potential errors deriving from the obstacle size estimation, localization system and path tracking controllers. As will be shown next, no safety margin would be required for the parking maneuvers planned with optimal control, since in the test scenarios presented in this work such maneuvers never lead to obstacle collisions.

[5] A low-pass filter is used to eliminate the high-frequency content of the path tracking error, to avoid rapid steering variations.

**TABLE 2.** CPU times of the optimal control problems on the four parking scenarios, using the grid of starting positions of Fig. 9.

| | Reverse Parking | Parallel Parking | Generic Parking Scenario | Angle Parking |
|---|---|---|---|---|
| **mean** CPU time solve **guess** | 1.01 s | 0.61 s | 0.62 s | 1.04 s |
| **max** CPU time solve **guess** | 2.04 s | 0.79 s | 1.15 s | 2.03 s |
| **mean** CPU time solve **OCP** | 1.10 s | 1.08 s | 0.54 s | 1.03 s |
| **max** CPU time solve **OCP** | 3.01 s | 2.95 s | 0.86 s | 2.51 s |
| **mean** CPU time solve **guess + OCP** | **2.11** s | **1.69** s | **1.16** s | **2.07** s |
| **max** CPU time solve **guess + OCP** | **4.45** s | **3.57** s | **1.82** s | **4.23** s |

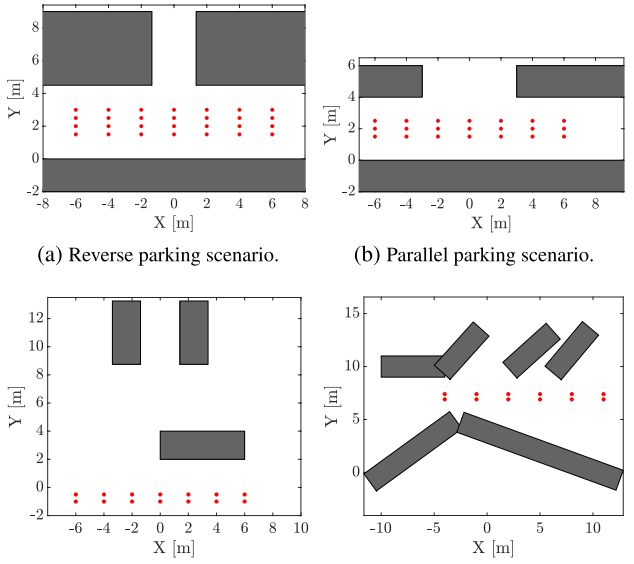


(a) Reverse parking scenario. (b) Parallel parking scenario.

(c) Generic parking scenario. (d) Angle parking scenario.

**FIGURE 9.** Grid of starting positions (red dots) used to test the automated parking framework, for each of the four parking scenarios. The total number of parking maneuvers is $28 + 21 + 14 + 12 = 75$.

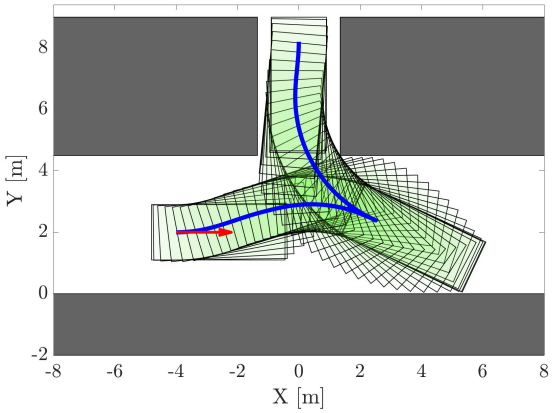


(a) Starting position before the target parking spot.

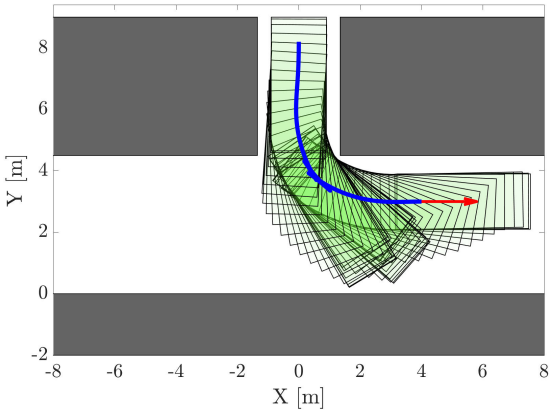


(b) Starting position after the target parking spot.

**FIGURE 10.** Reverse parking maneuvers, plotted for 2 of the 28 starting positions in Fig. 9a. The blue line represents the path of the vehicle reference point (center of the rear axle). The red arrow indicates the vehicle's forward direction at the starting point. Frames of the vehicle motion are shown every 10 discretization grid points of the OCP solution.

### *B. TRAJECTORY PLANNING SOLUTIONS WITH OPTIMAL CONTROL*

In this section, we show the trajectories planned with optimal control, for the four test scenarios previously described.

Fig. 10, 11, 12 and 13 depict some of the planned maneuvers, respectively for the reverse parking, parallel parking, generic parking and angle parking scenarios. For the sake of brevity, in each scenario, the parking maneuvers are plotted for only two of the many starting positions of Fig. 9. In each plot of Fig. 10, 11, 12 and 13, we show in green a sequence of 50 frames of the vehicle motion. The discretization time grid in the OCP contains 500 points, and it is therefore 10 times denser than the plotted sequence of frames.

The presented framework is able to plan complex maneuvers, composed of several segments with different travel directions. For example, the angle parking maneuvers in Fig. 13a and 13b have 4 segments, with the travel direction sequence forward-rearward-forward-rearward, while the reverse parking maneuver in Fig. 10b consists of 5 segments.

No collisions occur with the obstacles, in all the 75 testing scenarios. Such an accurate collision-free trajectory optimization is made possible by the dense mesh with which

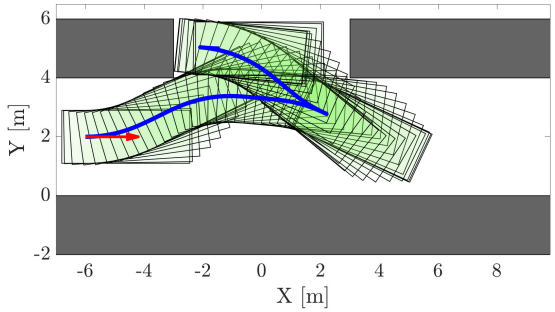


(a) Starting position before the target parking spot.

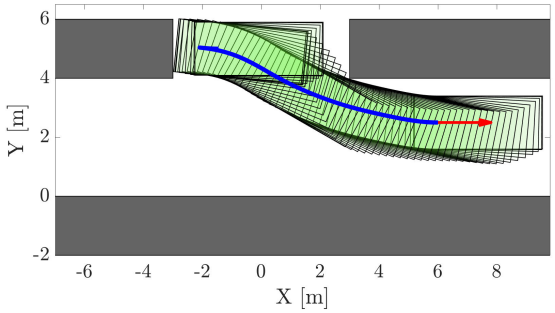


(b) Starting position after the target parking spot.

**FIGURE 11. Parallel parking maneuvers, plotted for 2 of the 21 starting positions in Fig. 9b. The blue line represents the path of the vehicle reference point (center of the rear axle). The red arrow indicates the vehicle's forward direction at the starting point. Frames of the vehicle motion are shown every 10 discretization grid points of the OCP solution.**

the OCPs are discretized, and by the relatively large number of collision-checking points. In contrast, the authors of [17] obtained simpler parking maneuvers, always composed of 2 segments, and their trajectories sometimes had local obstacle collisions between adjacent mesh points, due to a quite coarse discretization.

The OCPs are solved on a 2019 MacBook Pro, equipped with a 2,6 GHz 6-Core Intel Core i7 processor. Table 2 reports the computational (CPU) times to calculate the solution guesses (Section III-D) and solve the OCPs. On average, the CPU time to plan the parking maneuvers is around 1.5-2 s, and it is below 4.5 s for all the 75 tested maneuvers.

The main factors and novelties that contribute to decreasing the CPU times are:

- The formulation of the obstacle smooth penalty functions (Section III-B);
- The effectiveness of the solution guess strategy (Section III-D);
- The effectiveness of the PINS solver (Section III-C).

Table 3 compares the CPU times obtained with our *Hybrid A* + OCP tracking* guess strategy (Section III-D), against the Hybrid A* alone. The latter is used as a solution guess for optimal control by other authors, like [17]. However, the Hybrid A* returns only a feasible (often non-time-optimal) path, without speed and steering angle profiles. Conversely, our guess strategy uses the optimal control problem (12) to track the Hybrid A* path, and the resulting solution is then

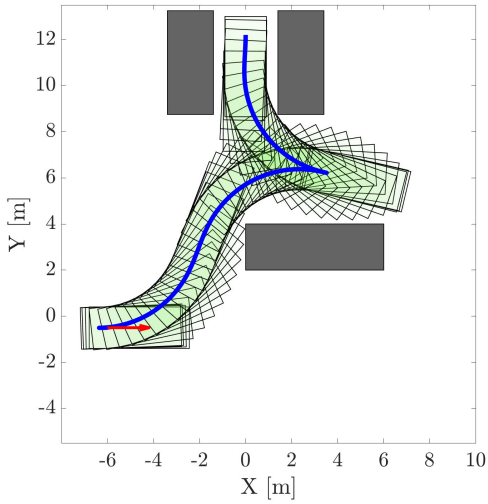


(a) Starting position before the obstacle.

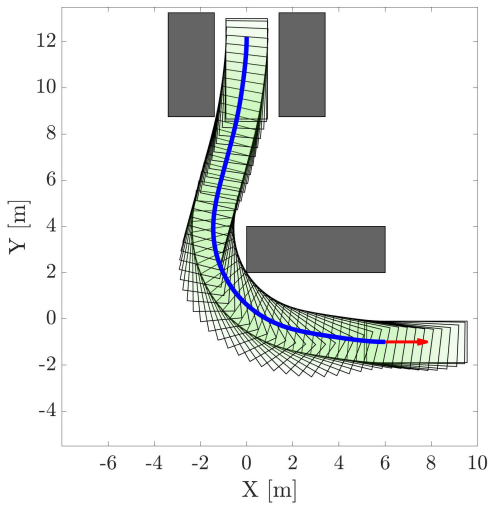


(b) Starting position after the obstacle.

**FIGURE 12. Generic parking scenario, plotted for 2 of the 14 starting positions in Fig. 9c. The blue line represents the path of the vehicle reference point (center of the rear axle). The red arrow indicates the vehicle's forward direction at the starting point. Frames of the vehicle motion are shown every 10 discretization grid points of the OCP solution.**

used as a guess for all the states and controls of the main OCP (11a)-(11e). Table 3 compares the mean CPU times obtained with our guess strategy and with the Hybrid A*, using the 75 parking maneuvers of the 4 scenarios (Fig. 9). Our guess method decreases by more than 20% the mean CPU times for trajectory planning (1.80 s against 2.30 s).

Assuming an automotive-grade hardware 5 times slower than the hardware employed in this paper, the scaled-up computational times to plan the parking maneuvers would still be acceptable for a commercial application.

### C. TRAJECTORY TRACKING WITH THE VEHICLE SIMULATOR

Following the scheme in Fig. 2, the parking trajectories planned with optimal control are tracked by low-level

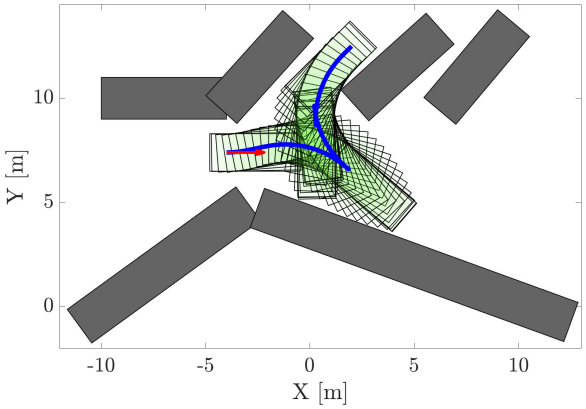


(a) Starting position before the target parking spot.

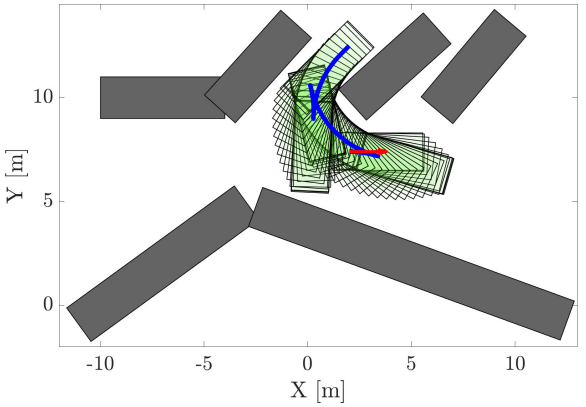


(b) Starting position after the target parking spot.

**FIGURE 13. Angle parking maneuvers, plotted for 2 of the 12 starting positions in Fig. 9d. The blue line represents the path of the vehicle reference point (center of the rear axle). The red arrow indicates the vehicle's forward direction at the starting point. Frames of the vehicle motion are shown every 10 discretization grid points of the OCP solution.**

**TABLE 3. Comparison of the proposed solution guess method, named *Hybrid A* + OCP tracking*, against the benchmark *Hybrid A** alone. The table compares the mean CPU times obtained on the four scenarios of Fig. 9 (75 parking maneuvers). Our method provides an improved guess to the OCP (11a)-(11e) for trajectory planning, whose overall mean computational time is decreased by more than 20% (1.80 s against 2.30 s).**

| | Hybrid A* | Hybrid A* + OCP tracking |
|---|---|---|
| mean CPU time solve **guess** | 0.50 s | 0.83 s |
| mean CPU time solve **guess + OCP** | 2.30 s | **1.80** s |

controllers (Section IV), to drive the high-fidelity vehicle simulator described in Section II-A. The trajectory tracking framework is implemented in a Matlab&Simulink environment.

A video demonstration of the planned and tracked parking maneuvers is available as supplementary material. The video was generated with the CARLA graphic environment [46]. However, we remark that we do *not* close the loop on the simple vehicle model of the CARLA simulator; on the contrary, we employ our high-fidelity vehicle simulator, illustrated in Section II-A.

**TABLE 4. Tracking performance on the four parking scenarios (75 parking maneuvers, whose starting conditions are shown in Fig. 9), with different low-level steering controllers. The proposed pNN+fb steering controller outperforms the literature benchmarks, in all the path and yaw angle ($\theta$) tracking error indicators. Considering the 0.10 m safety margin on the obstacle bounding boxes, pNN+fb is the only controller that never leads to collisions.**

| | Pure pursuit | Clothoid-based | pNN + fb |
|---|---|---|---|
| RMS(path track err) | 0.179 m | 0.015 m | **0.006** m |
| max(path track err) | 0.815 m | 0.164 m | **0.048** m |
| RMS($\lvert\theta - \hat{\theta}\rvert$) | 6.48 deg | 1.10 deg | **0.19** deg |
| max($\lvert\theta - \hat{\theta}\rvert$) | 20.52 deg | 5.02 deg | **0.74** deg |

### LITERATURE BENCHMARKS FOR STEERING CONTROL

The performance of the proposed feedforward-feedback pseudo-neural steering controller (Sections IV-A and IV-B) is compared with other two literature lateral controllers, namely the clothoid-based technique of [21] and the pure pursuit controller [22].

For the clothoid-based method [21], at each time step a clothoid curve is built, with the library developed by [47], to connect the current vehicle pose with a point on the target path, using a look-ahead distance of 2 m. The steering wheel angle computed by the clothoid-based controller at the time step $k$ is based on a kinematic relation:

$$\delta_{D_k} = f_{\text{st}}\Big(\arctan(\rho_{c_k} L)\Big) \tag{16}$$

where $\rho_{c_k}$ is the curvature value of the clothoid at its starting point, $L$ is the vehicle wheelbase, and $f_{\text{st}}(\cdot)$ is the vehicle (identified) steering map, described in Section IV-A.

For the pure pursuit controller, the look-ahead distance is tuned with experiments and set to 2.5 m.

### ANALYSIS OF THE TRAJECTORY TRACKING RESULTS

Table 4 compares the path and yaw angle tracking performance of the proposed feedforward-feedback steering controller (here named pNN+fb) with the clothoid-based and pure pursuit literature techniques. The comparison focuses on the root mean square (RMS) tracking errors and their maximum values, computed using the four parking scenarios and the 75 different starting positions shown in Fig. 9. The path tracking error (PTE) is computed as $\sqrt{(x_k - \hat{x}_k)^2 + (y_k - \hat{y}_k)^2}$, with $[\hat{x}_k, \hat{y}_k]$ being the real vehicle coordinates at time step $k$, and $[x_k, y_k]$ being the coordinates of the closest point on the optimal path. Similarly, the yaw angle tracking error is $\theta_k - \hat{\theta}_k$.

The proposed pNN+fb steering controller outperforms the literature benchmarks in all the path and yaw angle tracking error indicators. Considering that the maximum path tracking and yaw angle tracking errors obtained with the pNN+fb controller are 0.048 m and 0.74 deg respectively, and that the obstacle bounding boxes are defined with a safety margin of 0.10 m (Section V-A), then no collisions due to errors in the

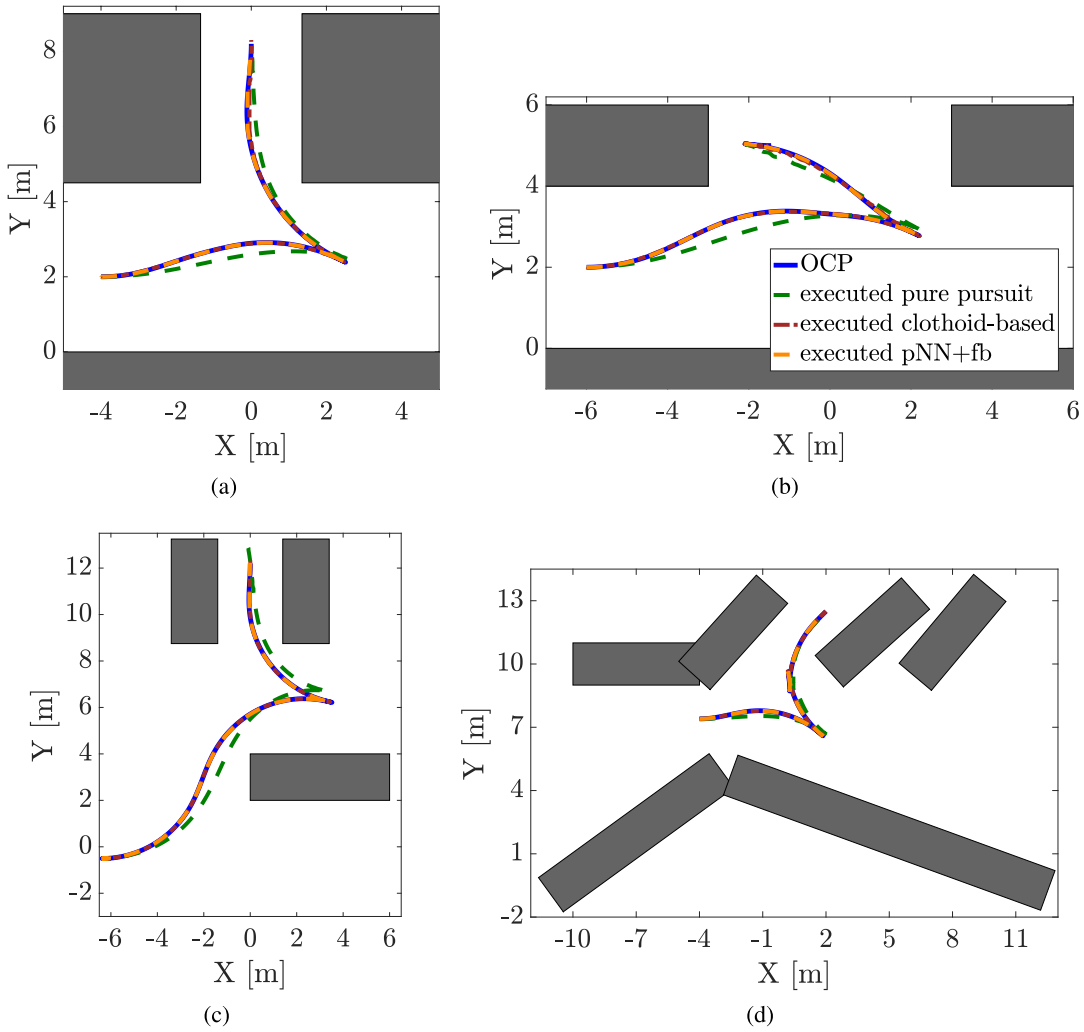


**FIGURE 14.** Comparison of the path tracking performance of the proposed feedforward-feedback pseudo-neural steering controller (pNN+fb) with the clothoid-based and pure pursuit literature techniques. The figure plots 4 of the 75 parking maneuvers considered in this paper: (a) reverse parking, (b) parallel parking, (c) generic parking scenario, (d) angle parking. The plots show the paths of the origin of the vehicle's reference frame, namely the center of the vehicle's rear axle.

tracking of the planned optimal path occur when the pNN+fb is used.

Fig. 14 shows some of the path-tracking results, in the four parking scenarios. Fig. 15 plots the forward speed $v_x$ and steering wheel angle $\delta_D$ profiles, together with the path and yaw angle tracking errors, for the parking maneuver of Fig. 14a. Note that the pNN+fb controller delivers a smooth steering angle $\delta_D$. Conversely, the clothoid-based and pure pursuit controllers sometimes yield oscillating or saturated steering angles, which result in worse tracking accuracy and decrease passenger comfort. Finally, the feedback longitudinal controller provides adequate speed-tracking performance.

The obtained results show that the presented framework is suitable for a real application, where planning and executing accurate maneuvers is fundamental, and the computational times should be reasonably low.

### D. ROBUSTNESS ANALYSES

#### 1) ROBUSTNESS TO VEHICLE AND ADHERENCE PARAMETERS

The framework's robustness is here analyzed by increasing the vehicle mass and reducing the road adherence, without changing the parameters of the trajectory planning and tracking controllers. Specifically, the vehicle mass is increased by 220 kg, and a wet road is simulated, decreasing by 40% the cornering and longitudinal tire stiffnesses [29], as well as the peak of the lateral and longitudinal tire forces. The changed vehicle and adherence parameters affect the curvature diagram (Fig. 8b) and the lateral dynamics, thus potentially decreasing the accuracy of the feedforward steering controller pNN. Nonetheless, the feedback steering controller compensates for part of the unmodeled dynamics, preserving good tracking accuracy. As reported in Table 5, the path and yaw angle tracking results do not degrade with

**TABLE 5.** Analyzing the effect of an unknown increase in the vehicle mass (by 220 kg) and road adherence reduction (by 40%) on the trajectory tracking performance. The table reports the path and yaw angle tracking errors on the four parking scenarios (75 parking maneuvers), obtained with the proposed pNN+fb steering controller. The results do not degrade with respect to the nominal case (Table 4), thus indicating good robustness of the automated parking framework to variations of the tyre-road adherence and/or vehicle physical properties.

| | Reverse Parking | Parallel Parking | Generic Parking Scenario | Angle Parking |
|---|---|---|---|---|
| RMS(path track err) | 0.007 m | 0.006 m | 0.008 m | 0.007 m |
| max(path track err) | 0.051 m | 0.043 m | 0.038 m | 0.055 m |
| RMS($\lvert\theta - \hat{\theta}\rvert$) | 0.20 deg | 0.23 deg | 0.15 deg | 0.22 deg |
| max($\lvert\theta - \hat{\theta}\rvert$) | 0.65 deg | 0.78 deg | 0.51 deg | 0.75 deg |

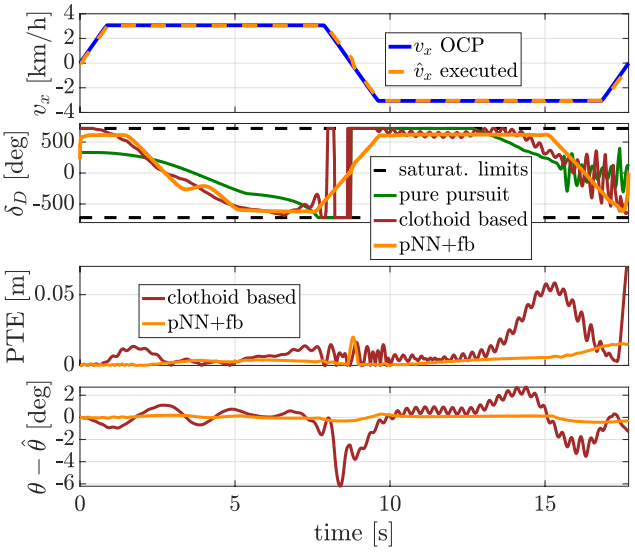


**FIGURE 15.** Trajectory tracking in the reverse parking scenario of Fig. 14a: speed ($v_x$) and steering angle ($\delta_D$) profiles, path tracking error (PTE) and yaw angle tracking error. The plots of the path and yaw tracking errors show only the two best controllers, excluding the pure pursuit. The proposed pNN+fb controller delivers a smooth steering angle $\delta_D$, while the clothoid-based and pure pursuit controllers sometimes yield oscillating or saturated steering angles, which result in worse tracking accuracy and decrease passenger comfort.

respect to the nominal case (Table 4), for the four parking scenarios and the 75 starting positions, which indicates good robustness of the automated parking framework to variations of the tyre-road adherence and/or vehicle physical properties.

### 2) ROBUSTNESS TO SENSOR NOISE

In this section, realistic sensor models are integrated into a state estimation setup, to evaluate the robustness of the planning and control framework to measurement noise. We remark that proposing an effective choice of sensors and localization techniques for autonomous parking is not in the scope of this paper. The state estimation methods in this section are used only to evaluate the results in the presence of measurement noise.

We define our parking scenarios using the *Automated Driving Toolbox* in Matlab & Simulink R2022b. Exploiting the Toolbox, the following sensors are simulated: a lidar, an inertial measurement unit (IMU) and wheel encoders. We stress that the sensors' selection is not the focus of this paper: in a real-world application, the lidar could be replaced by a radar, or by the combination of ultrasonic sensors and cameras. In our simulation environment, synthetic point clouds are generated by a lidar sensor mounted on the ego vehicle, using a realistic statistical model of the sensor detections. Simultaneous localization and mapping (SLAM) is performed with the Toolbox, using the lidar scans. The SLAM algorithm returns an estimate of the ego vehicle pose $[\hat{x}, \hat{y}, \hat{\theta}]$. In addition, an IMU model is used within the *imuSensor* function in Matlab, to measure the longitudinal and lateral accelerations $\hat{a}_x$, $\hat{a}_y$ and the yaw rate $\hat{\Omega} = \hat{\dot{\theta}}$. Finally, wheel encoder models are adopted to measure the angular rates of the four wheels, from which an estimate of the vehicle forward speed $\hat{v}_x$ is retrieved using the estimation algorithm described in [48, Chapter 5]. An extended Kalman filter (EKF) is implemented to fuse the available measurements, using a kinematic prediction model.

Fig. 16 shows the results obtained in the reverse parking scenario, with the state estimation setup previously described. The SLAM algorithm returns an estimate of the vehicle pose every 0.2 s (green dots in Fig. 16a), while the sampling time of the IMU and wheel encoders is 0.01 s. The EKF estimates the vehicle state (pose, velocities and accelerations) every 1 ms, and the estimates are fed to the tracking controllers. The RMS value of the path tracking error (PTE, Fig. 16b) between the desired and executed paths is 0.029 m, while its maximum value is 0.089 m. Considering the 0.10 m safety margin used to define the obstacle bounding boxes (Section V-A), no collisions occur throughout the maneuver execution. The estimates of forward speed $v_x$ and yaw rate $\Omega$ provided by the EKF are sufficiently close to the actual values (Fig. 16b), which results in a good tracking of the desired speed.

The feedback steering controller computes steering corrections $\delta_{\text{fb}}$ (Fig. 16b, dark-blue line of the bottom plot) to compensate for part of the path and yaw angle estimated tracking errors. Note that the overall steering wheel angle $\delta_{\text{ff}} + \delta_{\text{fb}}$ (orange line) remains sufficiently smooth, which is important for passengers' comfort. A rigorous stability analysis for the feedback steering controller is hindered by the nonlinear and black-box nature of the vehicle simulator, and by the presence of a nonlinear feedforward steering controller. Nonetheless, we remark that the feedback steering controller adds minor control corrections $\delta_{\text{fb}}$ (Fig. 16b,

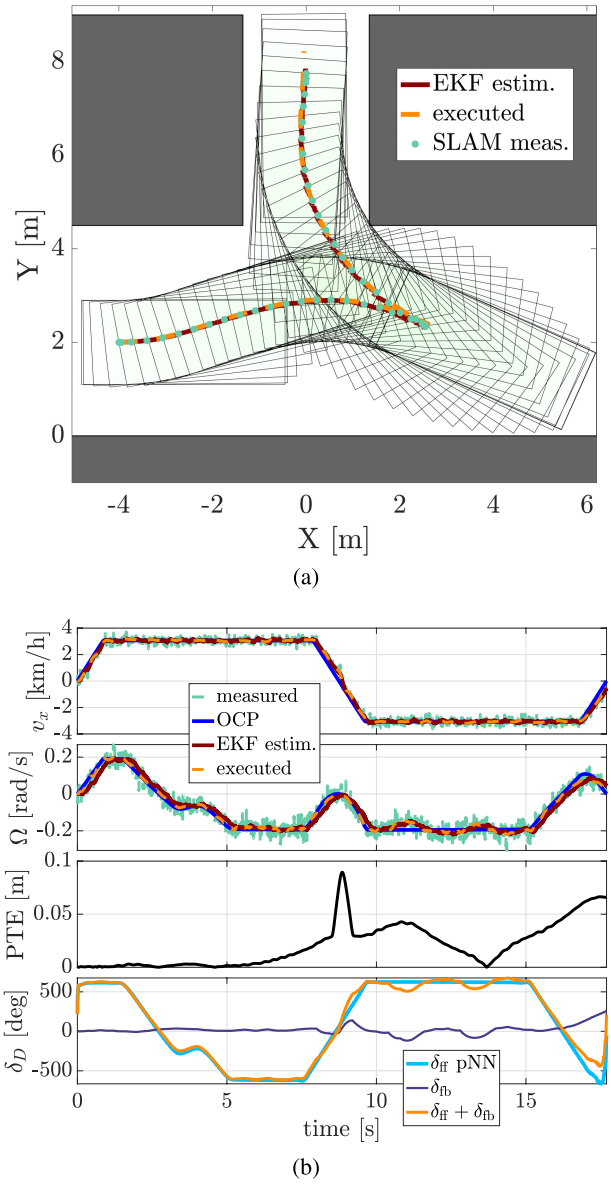


**FIGURE 16.** Executing a parking maneuver in the reverse parking scenario, in the presence of measurement noise: (a) comparison of the executed path with the raw SLAM results and the EKF estimates, and (b) forward speed ($v_x$), yaw rate, path tracking error (PTE) and steering wheel angle ($\delta_D$) profiles.

bottom plot), since most of the control action is provided by the feedforward steering controller pNN. The feedback steering controller considerably reduces the path and yaw angle tracking errors, in all the tested parking scenarios, even in the presence of unknown changes in the vehicle and adherence parameters. Thus, from a practical viewpoint, the feedback action improves the closed-loop tracking performance, and helps compensate for model mismatches and disturbances.

To limit the number of figures in the paper, we do not plot the results with measurement noise for all 4 parking scenarios (Fig. 14) and all 75 parking maneuvers. Nevertheless, our experiments demonstrate that the findings in Fig. 16 for the reverse parking scenario are representative of all parking scenarios. Even in the presence of synthetic measurement noise, obstacle collisions are consistently avoided.

## VI. CONCLUSION

In this paper, we presented a framework for fast planning and execution of complex autonomous parking maneuvers. Using an indirect optimal control approach, a minimum-time parking problem was formulated, and a novel smooth penalty function was adopted for collision avoidance with optimal control. We proposed an effective warm-start strategy for the optimal control problems, based on the creation of robust guess solutions by means of an optimal tracking of the path given by the Hybrid A* algorithm. A dense mesh was used to discretize the domain of the OCPs for trajectory planning, which yields accurate collision-free maneuvers.

We introduced a novel pseudo-neural feedforward-feedback steering controller, which, in comparison with other literature techniques, yields better accuracy and smoother steering angle profiles. Using the proposed steering controller and a feedback longitudinal velocity regulator, the planned maneuvers were executed in real-time with a 14-degree-of-freedom vehicle simulator.

The framework was validated using narrow reverse, parallel and angle parking spots, and more generic parking scenarios. The results show that our framework can plan and execute a wide range of parking maneuvers in different challenging scenarios, moving close to the obstacles and avoiding collisions. In addition, our optimal control formulation and solution method can compute maneuvers with multiple segments of forward and reverse driving. The framework is sufficiently robust to a change in the vehicle mass and in the tire-ground adherence. Moreover, collision-free maneuvers were executed in the presence of synthetic measurement noise, generated with realistic sensor models. Finally, the computational times are sufficiently low, and the framework is promising for a real-world automotive application.

Future work will be focused on testing the framework with an instrumented commercial vehicle, to implement a valet and autonomous parking application.

## ACKNOWLEDGMENT

The authors would like to thank Alice Plebe for her help with the preparation of the final video, and the critical reviews of the manuscript, and also would like to thank Matteo Larcher, for the development of the vehicle simulator.

*(Edoardo Pagot and Mattia Piccinini contributed equally to this work.)*

## REFERENCES

[1] P. Ramaswamy, "IoT smart parking system for reducing green house gas emission," in *Proc. Int. Conf. Recent Trends Inf. Technol. (ICRTIT)*, Apr. 2016, pp. 1–6.

[2] B. Li, L. Fan, Y. Ouyang, S. Tang, X. Wang, D. Cao, and F.-Y. Wang, "Online competition of trajectory planning for automated parking: Benchmarks, achievements, learned lessons, and future perspectives," *IEEE Trans. Intell. Vehicles*, vol. 8, no. 1, pp. 16–21, Jan. 2023.

[3] D. Dolgov, S. Thrun, M. Montemerlo, and J. Diebel, "Path planning for autonomous vehicles in unknown semi-structured environments," *Int. J. Robot. Res.*, vol. 29, no. 5, pp. 485–501, Apr. 2010.

[4] J. Petereit, T. Emter, C. W. Frey, T. Kopfstedt, and A. Beutel, "Application of hybrid A* to an autonomous mobile robot for path planning in unstructured outdoor environments," in *Proc. 7th German Conf. Robot. (ROBOTIK)*, May 2012, pp. 1–6.

[5] S. Karaman and E. Frazzoli, "Optimal kinodynamic motion planning using incremental sampling-based methods," in *Proc. 49th IEEE Conf. Decis. Control (CDC)*, Dec. 2010, pp. 7681–7687.

[6] Y. Dong, Y. Zhong, and J. Hong, "Knowledge-biased sampling-based path planning for automated vehicles parking," *IEEE Access*, vol. 8, pp. 156818–156827, 2020.

[7] B. Li, L. Li, T. Acarman, Z. Shao, and M. Yue, "Optimization-based maneuver planning for a tractor-trailer vehicle in a curvy tunnel: A weak reliance on sampling and search," *IEEE Robot. Autom. Lett.*, vol. 7, no. 2, pp. 706–713, Apr. 2022.

[8] B. Li and Z. Shao, "A unified motion planning method for parking an autonomous vehicle in the presence of irregularly placed obstacles," *Knowl.-Based Syst.*, vol. 86, pp. 11–20, Sep. 2015.

[9] B. Li, K. Wang, and Z. Shao, "Time-optimal maneuver planning in automatic parallel parking using a simultaneous dynamic optimization approach," *IEEE Trans. Intell. Transp. Syst.*, vol. 17, no. 11, pp. 3263–3274, Nov. 2016.

[10] C. Chen, B. Wu, L. Xuan, J. Chen, T. Wang, and L. Qian, "A trajectory planning method for autonomous valet parking via solving an optimal control problem," *Sensors*, vol. 20, no. 22, p. 6435, Nov. 2020.

[11] W. Sheng, B. Li, and X. Zhong, "Autonomous parking trajectory planning with tiny passages: A combination of multistage hybrid A-star algorithm and numerical optimal control," *IEEE Access*, vol. 9, pp. 102801–102810, 2021.

[12] J. Lian, W. Ren, D. Yang, L. Li, and F. Yu, "Trajectory planning for autonomous valet parking in narrow environments with enhanced hybrid A* search and nonlinear optimization," *IEEE Trans. Intell. Vehicles*, vol. 8, no. 6, pp. 3723–3734, Jun. 2023.

[13] B. Li, T. Acarman, Y. Zhang, Y. Ouyang, C. Yaman, Q. Kong, X. Zhong, and X. Peng, "Optimization-based trajectory planning for autonomous parking with irregularly placed obstacles: A lightweight iterative framework," *IEEE Trans. Intell. Transp. Syst.*, vol. 23, no. 8, pp. 11970–11981, Aug. 2022.

[14] S. Song, H. Chen, H. Sun, M. Liu, and T. Xia, "Time-optimized online planning for parallel parking with nonlinear optimization and improved Monte Carlo tree search," *IEEE Robot. Autom. Lett.*, vol. 7, no. 2, pp. 2226–2233, Apr. 2022.

[15] J. Zhang, H. Chen, S. Song, and F. Hu, "Reinforcement learning-based motion planning for automatic parking system," *IEEE Access*, vol. 8, pp. 154485–154501, 2020.

[16] S. Song, H. Chen, H. Sun, and M. Liu, "Data efficient reinforcement learning for integrated lateral planning and control in automated parking system," *Sensors*, vol. 20, no. 24, p. 7297, Dec. 2020.

[17] X. Zhang, A. Liniger, and F. Borrelli, "Optimization-based collision avoidance," *IEEE Trans. Control Syst. Technol.*, vol. 29, no. 3, pp. 972–983, May 2021.

[18] B. Paden, M. Cáp, S. Z. Yong, D. Yershov, and E. Frazzoli, "A survey of motion planning and control techniques for self-driving urban vehicles," *IEEE Trans. Intell. Vehicles*, vol. 1, no. 1, pp. 33–55, Mar. 2016.

[19] N. H. Amer, H. Zamzuri, K. Hudha, and Z. A. Kadir, "Modelling and control strategies in path tracking control for autonomous ground vehicles: A review of state of the art and challenges," *J. Intell. Robot. Syst.*, vol. 86, no. 2, pp. 225–254, May 2017.

[20] Y. Kebbati, N. Ait-Oufroukh, D. Ichalal, and V. Vigneron, "Lateral control for autonomous wheeled vehicles: A technical review," *Asian J. Control*, vol. 25, no. 4, pp. 2539–2563, Jul. 2023.

[21] D. Piscini, E. Pagot, G. Valenti, and F. Biral, "Experimental comparison of trajectory control and planning algorithms for autonomous vehicles," in *Proc. 45th Annu. Conf. IEEE Ind. Electron. Soc. (IECON)*, vol. 1, Oct. 2019, pp. 5217–5222.

[22] V. Sukhil and M. Behl, "Adaptive lookahead pure-pursuit for autonomous racing," 2021, *arXiv:2111.08873*.

[23] Z. Zhang, L. Xie, and H. Su, "Trajectory tracking control for autonomous parking using reduced-horizon model predictive control," in *Proc. 4th CAA Int. Conf. Veh. Control Intell. (CVCI)*, Dec. 2020, pp. 401–405.

[24] J. Zhang, Z. Shi, X. Yang, and J. Zhao, "Trajectory planning and tracking control for autonomous parallel parking of a non-holonomic vehicle," *Meas. Control*, vol. 53, nos. 9–10, pp. 1800–1816, Nov. 2020.

[25] B. S. Park, "Prescribed performance function based control for trajectory tracking of nonholonomic mobile robots with collision avoidance," in *Proc. IEEE Conf. Control Technol. Appl. (CCTA)*, Aug. 2017, pp. 1013–1018.

[26] S. He, S.-L. Dai, Z. Zhao, T. Zou, and Y. Ma, "UDE-based distributed formation control for MSVs with collision avoidance and connectivity preservation," *IEEE Trans. Ind. Informat.*, early access, May 22, 2023, doi: 10.1109/TII.2023.3274234.

[27] P. Zips, M. Böck, and A. Kugi, "Fast optimization based motion planning and path-tracking control for car parking," *IFAC Proc. Volumes*, vol. 46, no. 23, pp. 86–91, 2013.

[28] J. Moon, I. Bae, and S. Kim, "An inverse vehicle model for a neural-network-based integrated lateral and longitudinal automatic parking controller," *Electronics*, vol. 8, no. 12, p. 1452, Dec. 2019.

[29] H. Pacejka, *Tire and Vehicle Dynamics*, 3rd ed. Amsterdam, The Netherlands: Elsevier, 2012.

[30] D. Stocco and E. Bertolazzi, "Acme: A small 3D geometry library," *SoftwareX*, vol. 16, Dec. 2021, Art. no. 100845.

[31] M. Piccinini, S. Taddei, M. Larcher, M. Piazza, and F. Biral, "A physics-driven artificial agent for online time-optimal vehicle motion planning and control," *IEEE Access*, vol. 11, pp. 46344–46372, 2023.

[32] D. Stocco, M. Larcher, and E. Bertolazzi, "A novel approach for real-time tire/ground contact modeling," 2023.

[33] E. Bertolazzi, F. Biral, and M. Da Lio, "Symbolic–numeric indirect method for solving optimal control problems for large multibody systems," *Multibody Syst. Dyn.*, vol. 13, no. 2, pp. 233–252, Mar. 2005, doi: 10.1007/s11044-005-3987-4.

[34] E. Bertolazzi, F. Biral, and M. Da Lio, "Symbolic-numeric efficient solution of optimal control problems for multibody systems," *J. Comput. Appl. Math.*, vol. 185, no. 2, pp. 404–421, Jan. 2006. [Online]. Available: https://www.sciencedirect.com/science/article/pii/S0377042705001238

[35] E. Bertolazzi, F. Biral, and M. D. Lio, "Real-time motion planning for multibody systems: Real life application examples," *Multibody Syst. Dyn.*, vol. 17, nos. 2–3, pp. 119–139, Apr. 2007.

[36] F. Biral, E. Bertolazzi, and P. Bosetti, "Notes on numerical methods for solving optimal control problems," *IEEJ J. Ind. Appl.*, vol. 5, no. 2, pp. 154–166, 2016.

[37] N. Dal Bianco, E. Bertolazzi, F. Biral, and M. Massaro, "Comparison of direct and indirect methods for minimum lap time optimal control problems," *Vehicle Syst. Dyn.*, vol. 57, no. 5, pp. 665–696, May 2019, doi: 10.1080/00423114.2018.1480048.

[38] M. Piccinini, M. Larcher, E. Pagot, D. Piscini, L. Pasquato, and F. Biral, "A predictive neural hierarchical framework for on-line time-optimal motion planning and control of black-box vehicle models," *Vehicle Syst. Dyn.*, vol. 61, no. 1, pp. 83–110, Jan. 2023.

[39] E. Pagot, M. Piccinini, and F. Biral, "Real-time optimal control of an autonomous RC car with minimum-time maneuvers and a novel kineto-dynamical model," in *Proc. IEEE/RSJ Int. Conf. Intell. Robots Syst. (IROS)*, Oct. 2020, pp. 2390–2396.

[40] R. Lot and N. Dal Bianco, "Lap time optimisation of a racing go-kart," *Vehicle Syst. Dyn.*, vol. 54, no. 2, pp. 210–230, Feb. 2016.

[41] N. Dal Bianco, R. Lot, and M. Gadola, "Minimum time optimal control simulation of a GP2 race car," *Proc. Inst. Mech. Eng., D, J. Automobile Eng.*, vol. 232, no. 9, pp. 1180–1195, Aug. 2018.

[42] M. Da Lio, R. Donà, G. P. R. Papini, F. Biral, and H. Svensson, "A mental simulation approach for learning neural-network predictive control (in self-driving cars)," *IEEE Access*, vol. 8, pp. 192041–192064, 2020.

[43] M. D. Lio, M. Piccinini, and F. Biral, "Robust and sample-efficient estimation of vehicle lateral velocity using neural networks with explainable structure informed by kinematic principles," *IEEE Trans. Intell. Transp. Syst.*, early access, Aug. 21, 2023, doi: 10.1109/TITS.2023.3303776.

[44] T. Dozat, "Incorporating Nesterov momentum into Adam," in *Proc. ICLR*, 2016, pp. 1–4.

[45] J.-X. Xu and D. Huang, "Optimal tuning of PID parameters using iterative learning approach," in *Proc. IEEE 22nd Int. Symp. Intell. Control*, Oct. 2007, pp. 226–231.

[46] A. Dosovitskiy, G. Ros, F. Codevilla, A. Lopez, and V. Koltun, "CARLA: An open urban driving simulator," in *Proc. 1st Annu. Conf. Robot Learn.*, 2017, pp. 1–16.

[47] E. Bertolazzi and M. Frego, "Interpolating clothoid splines with curvature continuity," *Math. Methods Appl. Sci.*, vol. 41, no. 4, pp. 1723–1737, Mar. 2018. [Online]. Available: https://onlinelibrary.wiley.com/doi/abs/10.1002/mma.4700
[48] S. Savaresi and M. Tanelli, *Active Braking Control Systems Design for Vehicles*. London, U.K.: Springer, Jan. 2011, doi: 10.1007/978-1-84996-350-3.

**EDOARDO PAGOT** received the M.S. degree in mechatronics engineering and the Ph.D. degree (cum laude) in mechatronics engineering from the University of Trento, Italy, in 2018 and 2023, respectively.

He is currently a Research Fellow with the Department of Industrial Engineering, University of Trento. His research interests include multi-body dynamics modeling and optimal control (online and offline) in the field of vehicle dynamics, for both intelligent transportation and motorsport sectors.

**MATTIA PICCININI** (Member, IEEE) received the B.Sc. degree (cum laude) in industrial engineering and the M.Sc. degree (cum laude) in mechatronics engineering from the University of Trento, Italy, in 2017 and 2019, respectively, where he is currently pursuing the Ph.D. degree.

From March 2022 to June 2022, he was a visiting Ph.D. student with Universität der Bundeswehr, Munich, Germany. His research interests include motion planning, control, and state estimation methods for autonomous vehicles.

**ENRICO BERTOLAZZI** received the master's degree (cum laude) in mathematics from the University of Trento, Italy. He is currently an Associate Professor in numerical analysis with the Department of Industrial Engineering, University of Trento. His research interests include numerical analysis and include the development of numerical algorithms for the numerical solution of optimal control problems mainly with indirect methods.

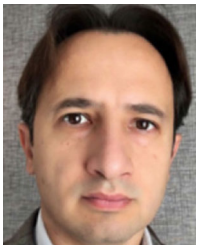

**FRANCESCO BIRAL** received the master's degree in mechanical engineering from the University of Padova, Italy, and the Ph.D. degree in mechanism and machine theory from the University of Brescia, Italy, in 2000, for his work on minimum lap time of racing vehicles with the use of optimal control.

He is currently an Associate Professor with the Department of Industrial Engineering, University of Trento. His research interests include symbolic and numerical multi-body dynamics and optimization, constrained optimal control, mainly in the field of vehicle dynamics with special focus on intelligent vehicles and optimal maneuver for racing vehicles. He has 15 years experience in the development and validation of ADAS and AD functions, both for cars and PTWs, gained in several European and industrial funded research projects.

Open Access funding provided by 'Università degli Studi di Trento' within the CRUI CARE Agreement